AGU PUBLICATIONS

JGR

Journal of Geophysical Research: Oceans

RESEARCH ARTICLE

10.1002/2013JC009279

Seasonal variability of the East Greenland Coastal Current

Sheldon Bacon[1], Abigail Marshall[2,3], N. Penny Holliday[1], Yevgeny Aksenov[1], and Stephen R. Dye[4,5]

[1]National Oceanography Centre, Southampton, UK, [2]Department of Ocean and Earth Sciences, University of Southampton, Southampton, UK, [3]Department of Animal and Plant Sciences, Sheffield University, Sheffield, UK, [4]Centre for Environment, Fisheries and Aquaculture Science, Lowestoft, UK, [5]School of Environmental Sciences, University of East Anglia, Norwich, UK

Key Points:

- The first measurements of the annual cycle of the East Greenland Coastal Current
- Modeled EGCC winter transports are double the summer values
- EGCC buoyancy and wind forcing are of similar importance

Correspondence to:
S. Bacon,
s.bacon@noc.ac.uk

Citation:
Bacon, S., A. Marshall, N. P. Holliday, Y. Aksenov, and S. R. Dye (2014), Seasonal variability of the East Greenland Coastal Current, *J. Geophys. Res. Oceans*, *119*, 3967–3987, doi:10.1002/2013JC009279.

Received 16 JUL 2013
Accepted 2 JUN 2014
Accepted article online 6 JUN 2014
Published online 25 JUN 2014

Abstract The East Greenland Coastal Current (EGCC) is characterized as cold, low-salinity polar waters flowing equatorward on the east Greenland shelf. It is an important conduit of freshwater from the Arctic Ocean, but our present understanding of it is poor, outside of an assortment of measurements which stem mainly from summertime visits by research vessels. This manuscript first describes measurements from moored instruments deployed on the East Greenland shelf (~63°N) between 2000 and 2004. The measurements are then used to show that a high-resolution coupled ice-ocean global general circulation model supports a realistic representation of the EGCC. The results show that the EGCC exists throughout the year and is stronger in winter than in summer. The model EGCC seawater transports are a maximum (minimum) in February (August), at 3.8 (1.9) × 10^6 m^3 s^{-1}. Freshwater transports, including modeled estimates of sea ice transport and referenced to salinity 35.0, are a maximum (minimum) in February (August) at 106 (59) × 10^3 m^3 s^{-1}. The model results show that wind and buoyancy forcing are of similar importance to EGCC transport. An empirical decomposition of the buoyancy-forced transport into a buoyancy-only component and a coupled wind and buoyancy component indicates the two to be of similar magnitude in winter. The model annual mean freshwater flux of ~80–90 × 10^3 m^3 s^{-1} approaches 50% of the net rate of Arctic freshwater gain, underlining the climatic importance of the EGCC.

1. Introduction

Changes in Arctic Ocean freshwater exports have the potential to change the oceans' thermohaline circulation [e.g., *Manabe and Stouffer*, 1995]. Therefore, it is important to understand the oceanic conduits for these freshwater exports. The largest liquid and solid freshwater export from the Arctic Ocean is through Fram Strait [*Koenigk et al*., 2007] where it either recirculates north of Denmark Strait [*Rudels et al*., 2002] or travels to Cape Farewell [*Sutherland et al*., 2009]. Liquid freshwater is transported in the East Greenland Current (EGC), which, south of Denmark Strait, is accompanied by the warmer, saltier Irminger Current to form the East Greenland Irminger Current (EGIC) [*Daniault et al*., 2011]. A second freshwater conduit is confined to the shelf and is known as the East Greenland Coastal Current (EGCC) [*Bacon et al*., 2002]. Existence of the EGCC south of Denmark Strait is clear but north of Denmark Strait is ambiguous [*Bacon et al*., 2008; *Sutherland and Pickart*, 2008].

Our present understanding of the EGCC is derived largely from summertime hydrographic sections. The EGCC carries cold ($\theta < 4°C$), fresh ($28 < S < 34$) polar water on the east Greenland shelf which sits over, and inshore of, ambient Atlantic waters ($S > 34.8$) [*Bacon et al*., 2002; *Sutherland and Pickart*, 2008]. The polar water ranges between 75 and 300 m thick at the coastline. It tapers offshore, reaching up to 45 km from the coast [*Sutherland and Pickart*, 2008]. At these low temperatures, salinity is an order of magnitude more important in controlling density than temperature, so the low EGCC salinities dominate horizontal density gradients and therefore (equatorward) geostrophic currents, which can reach speeds ~1 m s^{-1} [*Bacon et al*., 2002].

Summertime EGCC seawater transport estimates range between 0.5 and 2 Sv (1 Sv = 10^6 m^3 s^{-1}) [*Pickart et al*., 2005; *Wilkinson and Bacon*, 2005; *Holliday et al*., 2007]. A freshwater transport of 60 mSv was calculated by *Bacon et al*. [2002], and using a series of sections between Denmark Strait and Cape Farewell, *Sutherland and Pickart* [2008] found values up to double that. These freshwater transports are of considerable significance for climate: 60 mSv is equivalent to ~30% of the net Arctic rate of freshwater gain of ~0.2 Sv [*Dickson et al*., 2007; *Tsubouchi et al*., 2012]; and since the EGCC is a direct recipient of solid and liquid freshwater discharge from the Greenland ice sheet, its freshwater transport is likely to increase as ice sheet net ablation and seasonal meltwater runoff increase with time [see, for example, *Velicogna*, 2009; *Van den Broeke et al.*, 2009; *Shepherd et al.*, 2012]. Furthermore, the Cape Farewell retroflection [*Holliday et al.*, 2007] provides a fast and direct path for EGCC freshwater to the interior of the Subpolar Gyre, where the freshwater can decrease surface density, increase stratification, and thereby inhibit deep convection in the Irminger and Labrador Seas.

The only winter measurement (in March) comes from a drifter on sea ice which traveled quickly southwestward over the shelf south of Denmark Strait [*Bacon et al.*, 2008], but the seasonal variability of the EGCC is essentially unknown. It is plausible to imagine that the EGCC is strengthened, or even created, in the summer season by the enhanced density contrast resulting from increased freshwater input from sea and land ice melt. However, *Sutherland and Pickart* [2008] suggested the EGCC to be substantially wind forced and that it might even reverse in winter as a combined result of wind forcing and weak stratification.

The origin of the EGCC is also not entirely clear. Terrestrial meltwater runoff from Greenland has been hypothesized as a source of the EGCC freshwater signal [*Bacon et al.*, 2002]. *Sutherland and Pickart* [2008] hypothesized that the EGCC stems from the EGC at Kangerdlugssuaq Trough, a suggestion supported by the finding of a high Pacific water fraction within the upper 50 m of the EGCC [*Sutherland et al.*, 2009]. *Murray et al.* [2010] show satellite sea surface temperature measurements and postulate that the EGCC originates in the Kangerdlugssuaq catchment. *Våge et al.* [2013] produce a revised ocean circulation scheme north of Denmark Strait, which includes a bifurcation of the East Greenland Current, and it is possible that the inner branch may be relevant to the development of the EGCC.

There is evidence that the dominant contributor to the freshwater content of the EGCC is local melting of the sea ice exported through Fram Strait. *Bacon et al.* [2008] note that the annual mean surface winds blow equatorward, parallel to the coast of Greenland; therefore, sea ice traveling (roughly) southward down the east Greenland coast is driven toward the coast by Ekman transport. It melts as it proceeds southward and ambient temperatures increase. By this means, the EGCC may be supplied continually with additional freshwater, and it may be geographically constrained to lie adjacent to the coast. Oxygen isotope measurements on the East Greenland shelf are consistent with the view that the freshwater input to the EGCC mainly results from melting sea ice [*Cox et al.*, 2010].

Much remains to be learned about the EGCC. Our objectives within this manuscript are fourfold: (i) to describe 4 years of moored hydrographic measurements on the East Greenland shelf (~63°N, 40°W), which illuminate the seasonal variability of the EGCC; (ii) to use these measurements to query whether a high-resolution coupled ice-ocean general circulation model (GCM) is capable of representing adequately the EGCC; (iii) to use the GCM output to quantify the seasonal variation of seawater and freshwater transports in the EGCC; and (iv) to determine, from the GCM output, the relative importance of buoyancy and surface wind stress in forcing the EGCC. Section 2 describes the data, model, and methods; section 3 presents the results and addresses the first three objectives; and section 4 addresses the fourth objective and contains the discussion and conclusions.

2. Measurements, Model, and Methods

2.1. Moorings

These are challenging waters in which to deploy moorings. Sea ice cover limits access for a part of the year, and large icebergs calved from east Greenland glaciers pass down the coast. In an attempt to provide protection from icebergs, the moorings were tube deployments, which provide a walled protection to the instruments. The design allows the moorings to recover from knock-down as the tubes contain buoyancy spheres, so they are able to return to the nominal depth once the resistance from iceberg contact is removed. See *Holfort and Meincke* [2005] for further details of the design.

There has already been some limited use of the data described below. A simple estimate of the EGCC freshwater flux was made by *Dickson et al.* [2007] and *Holfort et al.* [2008] of 0.01–0.09 Sv. The high degree of uncertainty resulted from the use of a single current meter, the assumption of a barotropic current, and the lack of information on the width of the current. Also, *Murray et al.* [2010] used a simple time series of temperature and salinity derived from one of the moorings, with remote-sensed sea surface temperatures, in the context of Greenland ice sheet-ocean interactions.

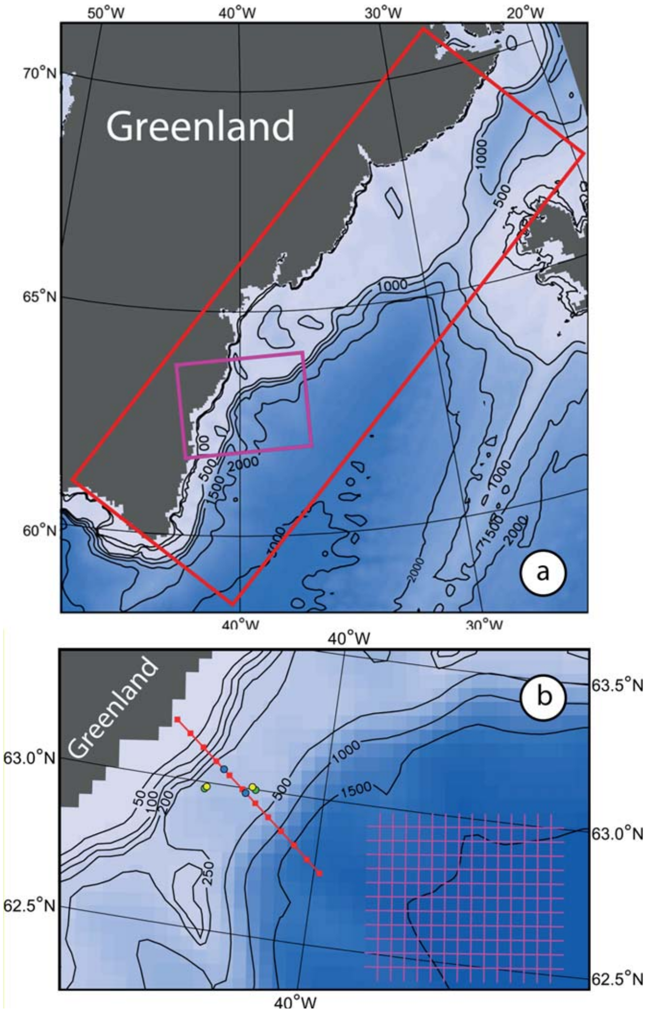

Figure 1. (a) South-eastern Greenland, with (large red box) the area of Figure 2 and (small pink box) the area of Figure 1b; (b) the study region, showing (green) the locations of the two moorings, (yellow) the grid cells used as virtual moorings, (blue) the projections of the virtual moorings onto (red) the model section; the pink grid illustrates the model grid. The background shows the model bathymetry; selected depths are labeled.

North of 63°N, the east Greenland shelf is relatively wide, so by deploying the moorings where the shelf narrows, it was hoped that a small array would capture as much of the freshwater pathway as possible. Historical hydrography was used to estimate the locations that would be most likely to sample most of the shallow freshwater surface layer through the year. Two moorings were deployed (Figure 1): an inner mooring at 62°58.6′N, 40°53.3′W, in water depth 294 m, and an outer mooring at 63°0.2′N, 40°32.7′W, in depths 300–303 m. The inner and outer locations were 18 km apart and approximately 20 and 35 km (respectively) from the Greenland coast. The line between the moorings was not normal to the trend of the coastline; rather, the outer lay north of east, relative to the inner.

The first deployment was of the outer mooring in August 2000. It was serviced annually, with final recovery in September 2004. The data span 4 years. The inner mooring was only deployed once, in July 2001. It was recovered 2 years later after an unsuccessful attempt the previous year. Unfortunately, subsequent tube mooring deployments at these locations were lost.

The first outer mooring deployment (2000–2001) had two Microcat SBE37-SM CTDs (conductivity-temperature-depth instrument) at nominal depths of 25 and 65 m. The instrumentation on both inner and outer moorings was increased for the later deployments, to one shallow Microcat CTD, two CT-only (conductivity and temperature) Microcats, and a Valeport 308 combined CTD and current meter. The nominal depths for the four instruments were 25, 45, 65, and 95 m. The temporal resolution varied between each instrument from 10 to 60 min. Typical temperature and salinity accuracies (for 2 year deployments) are 3 m °C and 0.1 psu. Mooring instrumentation and deployment details are summarized in Table 1.

The moorings that were retrieved had relatively limited damage with no resulting data loss. The first outer mooring deployment (2000–2001) had a broken tube on recovery. The buoyancy on the third deployment (2002–2003) appeared damaged, explaining the variable pressure record. Thirteen months into the inner mooring deployment (2001–2003), the mooring was dragged, likely by contact with an iceberg, and deposited in water ~40 m deeper.

Table 1. Technical Details for Mooring Deployments, 2000–2004[a]

Deployment	Latitude (N)	Longitude (W)	Inst.	Params.	Depth (m)	Start	End	Freq. (min)
Outer_00	63°0.2′	40°32.7′	M	CTD	25	Aug 2000	Jun 2001	60
			M	CTD	64	Aug 2000	Jun 2001	60
Outer_01	63°0.2′	40°32.7′	M	CTD	20	Jul 2001	Jun 2002	30
			M	CT	39	Jul 2001	Jun 2002[b]	10
			M	CT	59	Jul 2001	Jun 2002	10
			V	VCTD	97	Jul 2001	Dec 2001	10
Outer_02	63°0.1′	40°32.5′	M	CTD	26	Jun 2002	Jul 2003	10
			M	CT	45	Jun 2002	Jul 2003	10
			M	CT	64	Jun 2002	Jul 2003	10
			V	VCTD	98	Jun 2002	Nov 2002	20
Outer_03	63°0.2′	40°32.7′	M	CTD	22	Jul 2003	Sep 2004	10
			M	CT	41	Jul 2003	Sep 2004	10
			M	CT	60	Jul 2003	Sep 2004	10
			V	VCTD	93	Jul 2003	May 2004	20
Inner_13	62°58.6′	40°53.3′	M	CTD	17	Jul 2001	Jul 2003	30
			M	CT	36	Jul 2001	Jul 2003	10
			M	CT	55	Jul 2001	Jul 2003	10
			V	V	89	Jul 2001	Oct 2001	20

[a] Under *Instruments* (Inst.), M = Seabird SBE37-SM Microcat, and V = Valeport model V308 2-D current meter. Under *Parameters* (Params.), C = conductivity, T = temperature, D = depth, V = 2-D velocity. *Depth* is nominal depth. Instrument recording *start* and *end* months are given; instrument sampling frequency is *freq*. Note that mooring Inner_13 was presumed dragged by iceberg contact during August 2002, after which time, nominal depths increased by ~40 m.

[b] Salinity data from the CT at 39 m during Outer_01 deployment was used in the analysis up to January 2012 only.

2.2. Data Analysis

The top (Microcat) and bottom (current meter) instruments on the moorings carried pressure sensors, but the current meter measurements were of shorter duration and the two middle instruments (Microcats) carried no pressure sensors, so intermediate depths were calculated using linear interpolation. When the measured pressures from the upper and lower instruments were available, both were used to calculate the pressure for the intermediate sensors. The interpolation method was evaluated using the 2000–2001 outer mooring deployment, where both top and bottom instrument pressure records were complete, by calculating the differences in pressure resulting from using the top or bottom instrument alone compared with using both instruments. The resulting uncertainty was ±5 dbar.

For analysis of the data, temperature and salinity were gridded between 20 and 150 dbar with grid interval 10 dbar. Occasional knockdowns allowed us to take advantage of a greater depth range than the nominal depths for each instrument would have covered. Each record had 2, 3, or 4 in situ values, depending on the number of instruments per mooring; linear interpolation was then used to fill the grid. To inspect the seasonal cycle, data from each mooring were collated by calendar month and a grid file created between the given depths and covering January to December. To inspect representativeness from the perspective of interannual variability, time series of data from set depths, close to nominal instrument deployment depths, were extracted from the gridded file formed from the full time series.

2.3. Model Specification

The Nucleus for European Modeling of the Ocean (NEMO) is a widely used framework for oceanographic modeling. We describe results using NEMO version 3.3.1. NEMO uses the primitive equation model Ocean Parallelisé (OPA 9.1) [*Madec et al.*, 2011] coupled with the Louvain-la-Neuve sea ice model (LIM2) [*Fichefet et al.*, 1997]. The model is discretized on a tripolar grid with two northern poles (one in Siberia, one in Canada) and the geographical South Pole. A detailed bathymetry is used by modification of the 2 min gridded global relief Earth Topography (ETOPO2v2), which contains *Smith and Sandwell* [1997] satellite data between 72°N and 72°S, the International Bathymetric Chart of the Arctic Ocean (IBCAO) [*Jakobsson et al.*, 2008] above 72°N, and the 5 min gridded Digital Bathymetric Data Base (DBDB5) for south of 72°S. Description of ETOPO2v2 is available from the National Geophysical Data Center of the U. S. National Oceanic and Atmospheric Administration via their website at http://www.ngdc.noaa.gov/, and description of DBDB5 by the U. S. Naval Oceanographic Office via the Global Master Change Directory of the U. S. National Aeronautics and Space Administration website at http://gcmd.nasa.gov/.

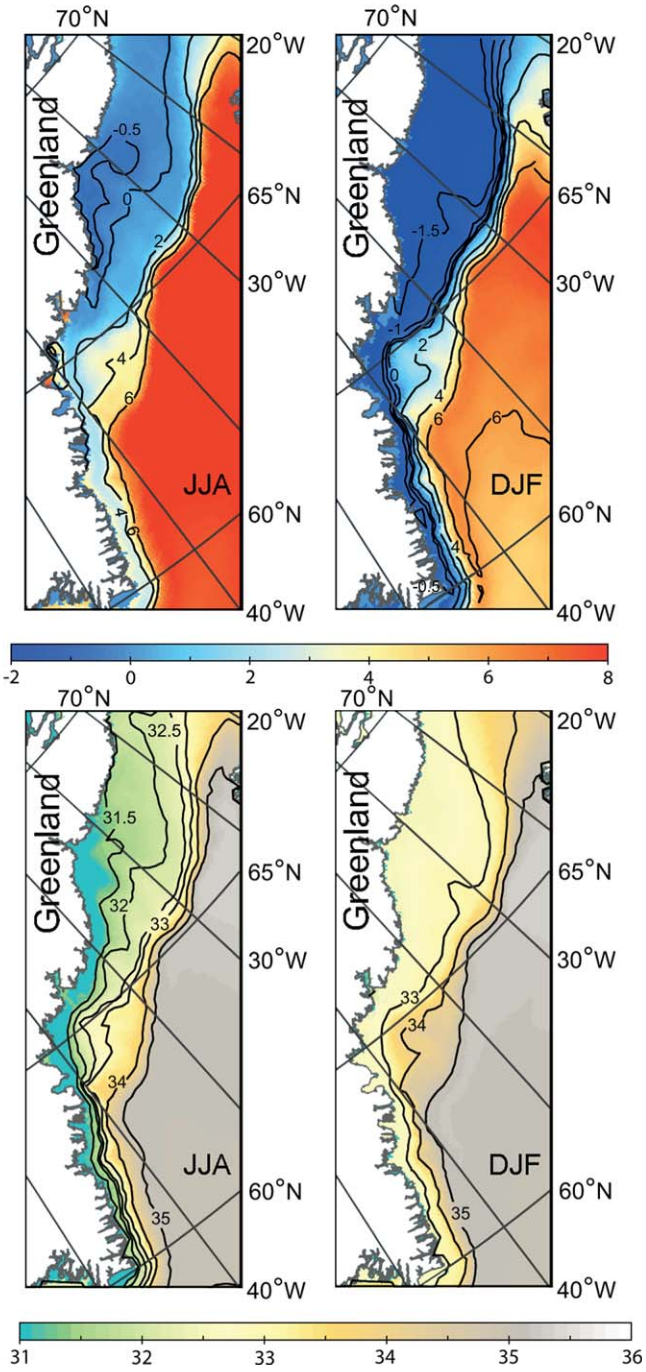

Figure 2. NEMO surface temperature (°C, above) and salinity (below) for summer (JJA) and winter (DJF).

The ocean free surface is nonlinear [*Levier et al.*, 2007]. Initial values of sea temperature and salinity are obtained from the World Ocean Atlas (WOA) [*Levitus et al.*, 1988a, 1988b] merged with the Polar Hydrographic Climatology PHC2.1 database [*Steele et al.*, 2001] in high latitudes. The sea surface salinity is relaxed toward the monthly mean from WOA, which has a resolution of 1° latitude by 1° longitude. The relaxation is equivalent to restoring model salinity to observed in the top 50 m on a time scale of 180 days. The surface salinity relaxation in the Arctic Ocean is equivalent to a surface freshwater flux of order 30 mSv, and it has no direct impact on ocean structure on scales smaller than O(100) km. Over the area shown as the red box in Figure 1a, the relaxation is equivalent to maximum (mean) surface freshwater flux of 1.5 (0.3) mSv.

Model atmospheric forcing is described by *Brodeau et al.* [2010]. Atmospheric features are drawn from the Common Ocean Reference Experiment (CORE2) and the European Centre for Medium-range Weather Forecasts (ECMWF). Air-sea and air-ice fluxes are calculated by atmospheric boundary layer formulations [*Large and Yeager*, 2004]. Meltwater runoff from ice sheets is not included.

With 1/12° mean horizontal resolution, this NEMO version (ORCA0083) is eddy resolving in most of the world ocean, so there is no parameterization for lateral mixing due to eddies. An isoneutral Laplacian operator is used for lateral tracer diffusion. A bi-Laplacian horizontal operator is applied for momentum diffusion. A turbulent kinetic energy (TKE) closure scheme is used for vertical mixing. It incorporates background values for vertical eddy viscosity of 10^{-4} m^2 s^{-2}, for vertical eddy diffusivity of 10^{-5} m^2 s^{-2}, and for TKE of 10^{-6} m^2 s^{-2} [*Madec et al.*, 2011]. Over the Greenland shelf where the Rossby radius is ~7 km [*Bacon et al.*, 2002], the model resolution is ~5 km and therefore is "eddy permitting." The horizontal grid is illustrated in Figure 1b. In the vertical, the model contains 75 levels from the surface to 5900 m, and layers increase in thickness from 1 m at the surface to 204 m at the bottom; 29

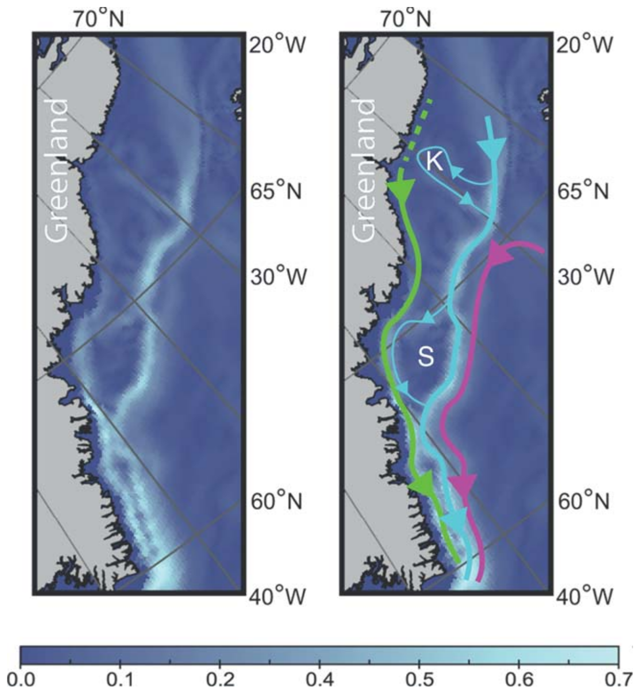

Figure 3. NEMO annual mean current speeds (m s^{-1}, color scale) at 47 m depth. Both plots are the same. The right plot overlays the main currents in sketch form: EGCC (green), EGC (cyan), with diversions onto the shelf, and the Irminger Current (pink). Two major bathymetric features are labeled: Kangerdlugssuaq Trough (K) and Sermilik Trough (S).

levels cover the first 150 m. In addition, partial steps in the model bottom topography are used to improve model approximation of the steep seabed relief near the continental shelves [*Barnier et al.*, 2006].

2.4. Model Output

Model output was analyzed from January 2000 to December 2007; the time period was chosen to provide some overlap with the measurement period and is well clear of the model start-up (1978). The output files were generated as 5 day averages which were then averaged into monthly means, without changing the horizontal or vertical resolution. To generate annual cycles, the 8 years of monthly mean model output were further averaged into mean calendar months. To compare seasonal differences, mean calendar months were averaged into summer (JJA) and winter (DJF) seasons. Horizontal area output was extracted from the region shown in Figure 1a. Output at the locations of two "virtual" moorings was extracted, using grid points as close as possible to the positions of the actual moorings, with geographical coordinates 62°59.8′N, 40°31.2′W and 62°58.7′N, 40°48.8′W. A section normal to the coast (and also to the mean currents), defined for proximity to the mooring locations, was extracted from the model.

3. Results

In this section, we will describe and compare the results from the measurements and the model. The section concludes with the calculation from the model section of transports of seawater, and liquid and solid freshwater.

3.1. Properties, Densities, and Velocities

The objectives of this manuscript would be moot if the model did not support a plausible representation of the EGCC. Model mean summer (JJA) and winter (DJF) surface temperature and salinity (Figure 2) show cold, fresh water on the east Greenland shelf. On-shelf temperatures are uniformly low in winter, while in summer they are still low but become warmer toward the south. Salinities are also uniform on-shelf in winter, but in summer there is a band of fresher water near the coast. Surface properties and seasonal changes resemble those shown in, e.g., *Dietrich* [1969]. Figure 3 shows model annual mean velocities (from 47 m depth). There is a striking similarity between this plot and the hypothesized circulation schematic of *Sutherland and Pickart* [2008, their Figure 16]. The model's EGCC is seen near the coast, apparently emerging on the shelf from the background around latitudes 67°N–68°N. The EGC is further offshore in deeper water but shows onshore excursions around topographic features—Kangerdlugssuaq and Sermilik Troughs. Finally, there is also the recirculating Irminger Current. This is clear evidence that the model represents the known regional circulation features. We note in passing that the EGCC's emergence is consistent with its being generated from sea ice melt, but further exploration of its source(s) and fate(s) are beyond the scope of the present manuscript.

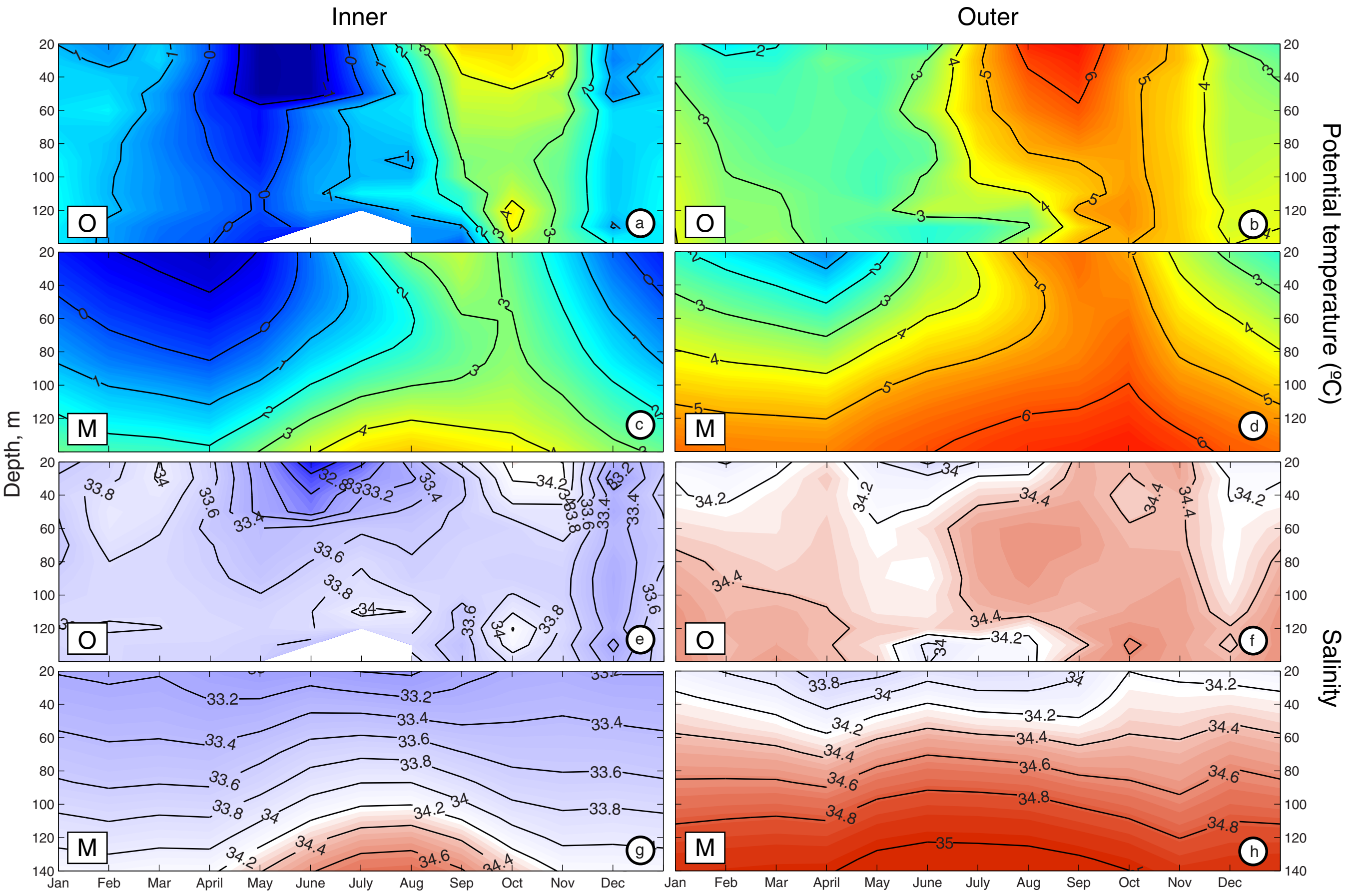

Figure 4. Seasonal cycles of temperature and salinity. Observations (O) and model output (M); (left) inner location and (right) outer location. (a–d) Temperature (°C) and (e–h) salinity.

We next examine the monthly mean measured and modeled seasonal cycles (i.e., aggregated into a single calendar year) in θ and S at both inner and outer locations over the available measured depth range (20–150 m; Figure 4). In both measurements and model output, the inner mooring is colder and fresher than the outer mooring. Annual mean (20–120 m depth) model properties are very similar to observations (Table 2): the differences (measurements minus model) of these annual means of θ and S at inner (outer) locations are 0.1 (-0.15) °C and 0.08 (0.00), respectively. Both model and observations show similar and pronounced seasonal cycles in temperature. At the inner location, maximum temperatures are seen near-surface around September. Minimum temperatures in the measurements appear near-surface around May-June, whereas modeled minima, while also near-surface, occur earlier, around February-March. At the outer location, both observed and modeled minima occur near surface around April. Observed and modeled maximum temperatures are seen at depth (~140 m), centered around late summer/early autumn, between July and October. A secondary, near-surface temperature maximum is centerd on September. Considering salinity, the measured and modeled annual cycles at the outer location are similar in timing and amplitude, with vertical salinity gradient strongest in summer (centered on July-August) and weakest in winter (around December-January). At the inner location, the clearest feature is the observed near-surface salinity minimum centered on June, the insolation maximum, and is a consequence of sea ice melt. This feature appears in the model output at the same time, but is much weaker. At other times and depths at this location, evidence of seasonality is less clear.

Interestingly, *Straneo et al*. [2010, their Figure 3] present an annual cycle of East Greenland shelf water temperature, from the surface to 400 m, January-December, obtained from tagged seals. The data come from the whole shelf, between coast and shelf break, and to the north of our study location, between 64°N and

Table 2. Measured and Modeled Annual Average Potential Temperature (θ, °C) and Salinity (S) for Inner and Outer Mooring Locations, Between 20 and 120 m Depth

	Property	Inner	Outer
Measured	θ	1.30	3.89
Modeled	θ	1.20	4.04
Measured	S	33.57	34.37
Modeled	S	33.49	34.37

68°N. Their plot is similar to our observed inner mooring annual cycle of temperature (Figure 4), with a surface-intensified minimum in May-June. Since the EGCC comprises inshore cold (and fresh) water with offlying warmer (and more saline) water, it may be that the two temperature modes are combined in this single plot and that a separation along the lines of *Sutherland et al*. [2013] would have been useful.

We pursue the observed and modeled seasonality by inspecting θ and S variability at fixed depths, in Figures 5 and 6 for the inner and outer moorings, respectively, where we now extract the monthly mean properties at fixed depths, by calendar year, set against the envelope of modeled variability. We choose two depths for comparison: the shallowest available from the observations (19 dbar) and a representative mid-depth value (97 dbar). We add a third envelope which is only available from the model output—the surface layer, at 1 dbar. First, this view confirms the conclusions drawn in the previous paragraph. Second, it is seen that the observed property variability is greater than modeled, by a factor ~2. Third, although we only have 1 year of observations at the shallowest depth for the inner mooring, we note that measured seasonal cycle in salinity at 19 m depth is similar in amplitude and phase to the modeled surface salinity at 1 m depth. It is possible that modeled near-surface turbulent mixing is too weak, inhibiting the downward propagation of the freshwater input from sea ice melt.

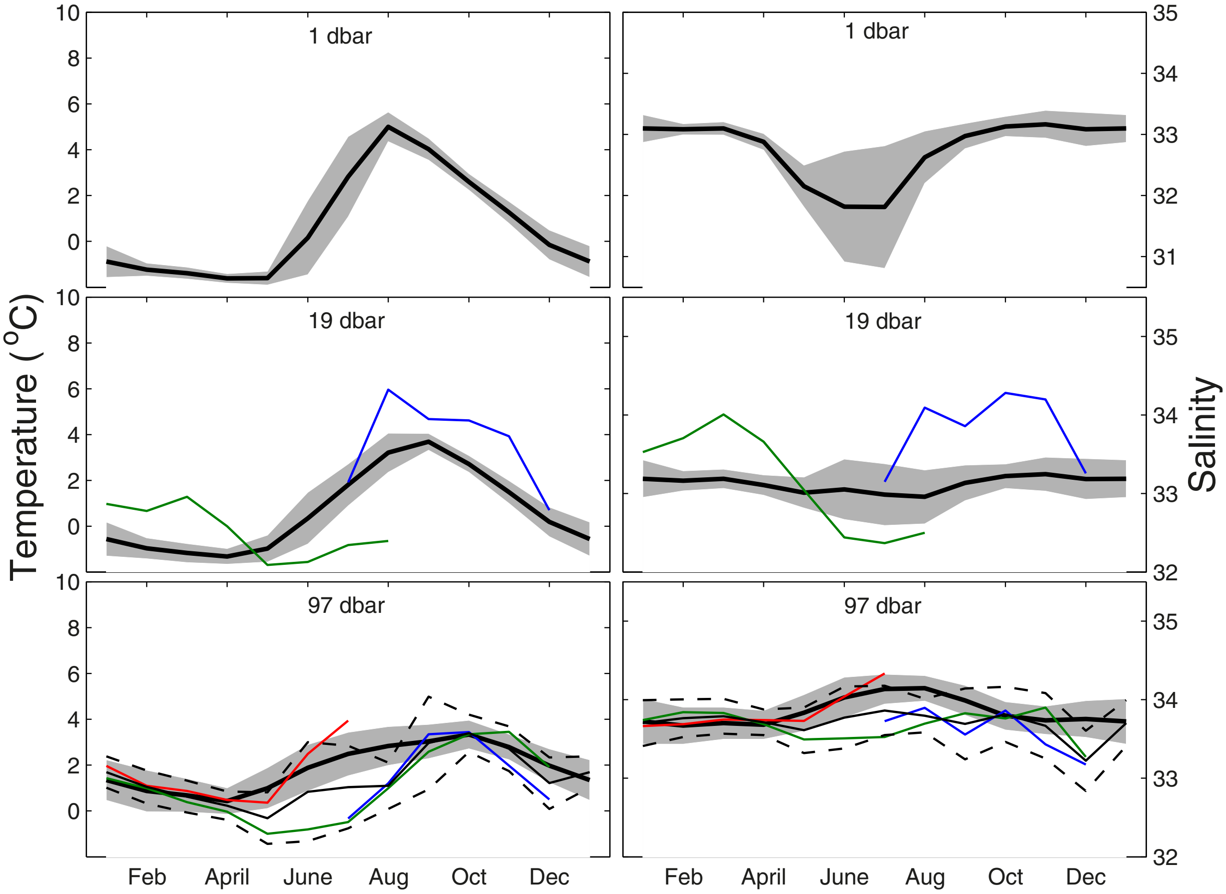

Figure 5. Inner location annual cycle of (left) temperature (°C) and (right) salinity at three depths (labeled). Model mean (thick black) ± 1 SD (gray envelope). Measurements are mean (thin black), 2001 (blue), 2002 (green), 2003 (red), ±1 SD (dashed line) for bottom plots.

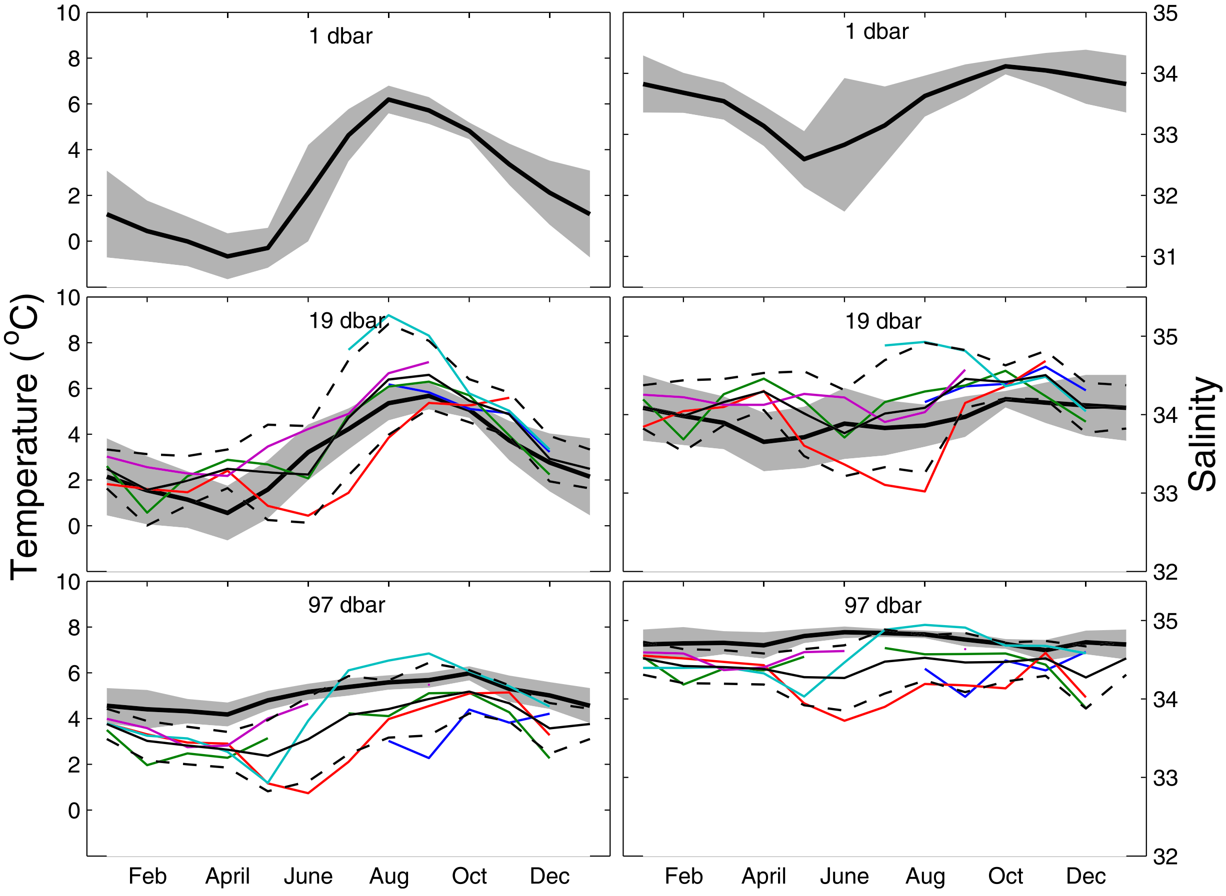

Figure 6. Outer location annual cycle of (left) temperature (°C) and (right) salinity at three depths (labeled). Model mean (thick black) ± 1 SD (gray envelope). Measurements are mean (thin black), 2000 (red), 2001 (green), 2002 (blue), 2003 (cyan), 2004 (magenta), ±1 SD (dashed line).

We next aggregate the observations and model output into mean profiles (±1 SD) of θ, S and density at both inner and outer locations (Figure 7). We only use observation depths where at least one full annual cycle is available. Also, we include the uppermost model levels which lie above the shallowest observations. The profiles of θ and S confirm the conclusion in the previous paragraph that the observed variability is greater than modeled. While there are differences between observed and modeled vertical property gradients, it is seen that the vertical density gradients are similar.

To summarize the preceding results, we show next θ-S diagrams for measured and modeled inner and outer locations, for winter (DJF) and summer (JJA; Figure 8). While the model output presents higher densities at depth (as previously noted), the modeled temperatures and salinities preserve the observed water mass characteristics to the extent that measurements and model output lay largely on the same lines (in winter) or exhibit similar scatter (in summer) through warming and freshening. It is interesting to note that in both summer and winter, the observations and model output both reach similar densities (given the scatter in properties) at the shallowest common depth (19 m). The consequence of summer surface warming is seen most clearly in the observations at the inner location: the turn to higher temperatures and lower salinities is replicated and extrapolated to the surface by the model. We conclude that the extrapolation to the surface provided by the model output can be considered plausibly realistic.

The two moorings had one common year for the shallowest instruments and two common years for the deepest instruments, so we now examine and compare horizontal density gradients in the model and in observations. They are presented in Figure 9 in the same style as Figures 5 and 6, by showing the model monthly mean envelope for two depths, with observed calendar-monthly values superimposed. All density

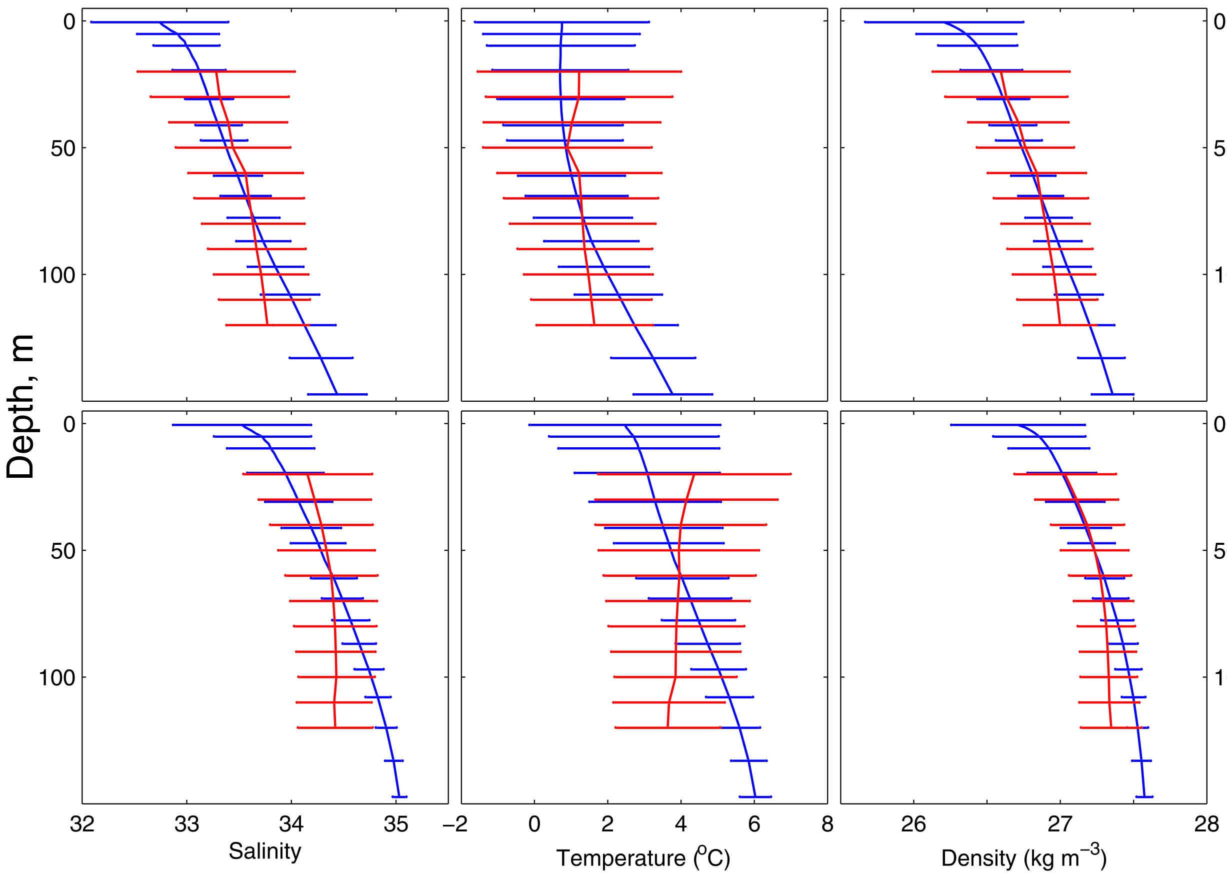

Figure 7. (top) Inner and (bottom) outer location mean salinity, temperature, and density (±1 SD) for measurements (red) and model (blue).

gradients are single-signed (positive), meaning here that the isopycnal surfaces always slope down toward the coast. Allowing for some observed month-to-month variability, the similarity between measurements and model at the greater of the two depths is remarkable. Almost the same mean values are seen in summer (July-August, low) and winter (January, high), and the observed mean tracks the model mean from summer to winter. The main difference between observations and model is in the development from winter to summer, where the observations decline while the model values remain elevated. Having noted above that the modeled near-surface salinity was similar to the measured salinity at 19 m, we choose to compare the shallowest observed gradient (19 m) with the modeled values from 5 m. The sense of the annual cycle is here reversed in comparison with the greater depth. The maximum is seen in summer, and the timing is similar for model and observations (July and June, respectively), as are the magnitudes. Also, the timing of the minimum is similar (April and March, respectively). The main difference is seen between August and March, where observed values are lower than the model output.

We turn now to the velocity measurements. The current meters were deployed at nominal depths between ~90 and 100 m, but the strong currents and occasional knock-downs meant that their depth varied continually between the nominal depth and up to 140 m. With only a single current meter on each mooring, there is no possibility to use interpolation to reduce the observations to a consistent (single) depth, and with only 1 (near) year long record, the others being just a few months in duration, we choose the simplest way to display the currents, as progressive vector diagrams (Figure 10). For the model output, we show a full year of average currents, starting in July to match with the observations. Both modeled locations and the short inner observation record show steady directions, approximately parallel to the coast and the bathymetry, but the outer observations in the long record show a clear component of velocity directed offshore, perpendicular to the coast. Also, the observations are divergent—the outer location is oriented more southerly

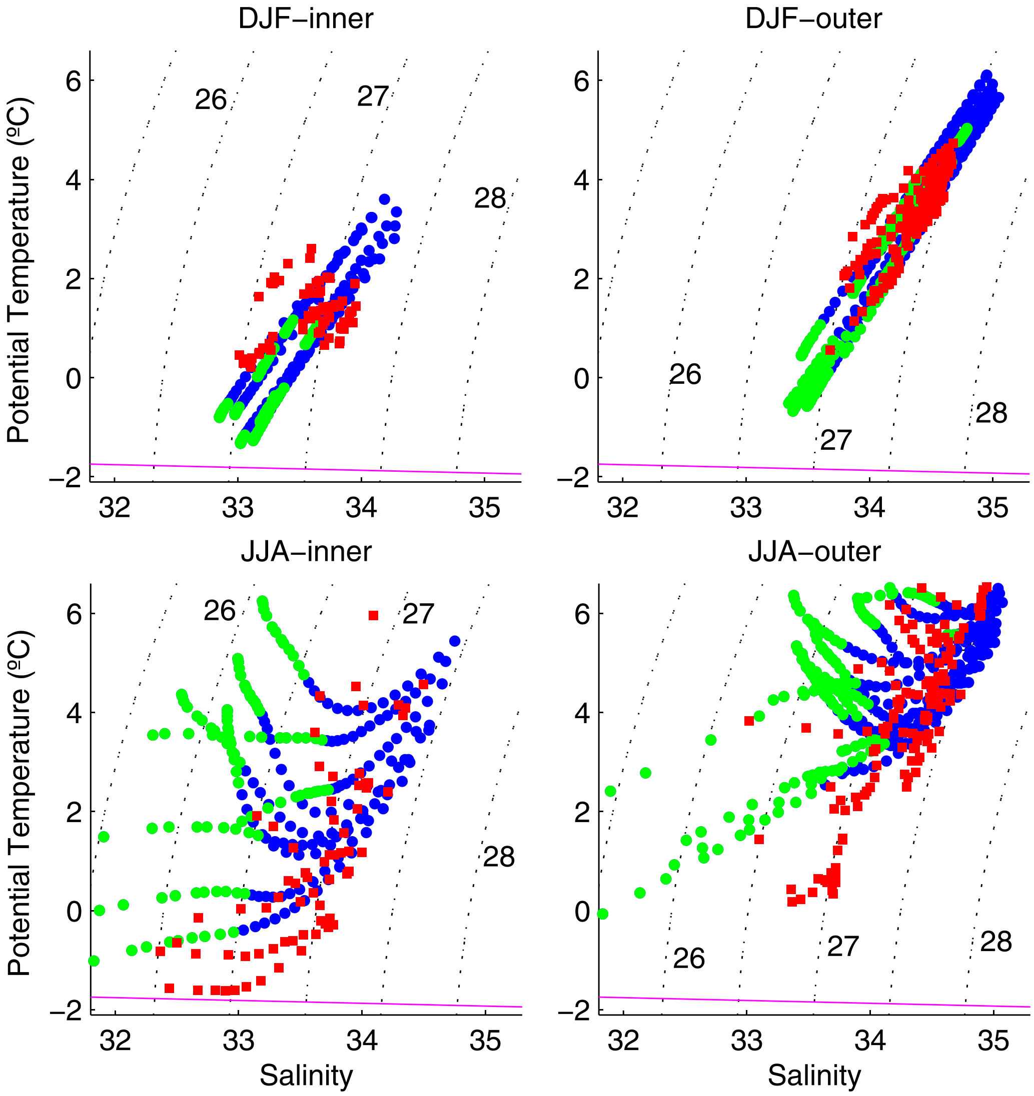

Figure 8. Potential temperature/salinity diagrams for winter (DJF) and summer (JJA), for inner and outer mooring locations, measured and modeled. Measurements (red) are plotted between 20 and 120 m depth. Model output is shown between 20–120 m depth (blue) and 0–20 m depth (green). Potential density (σ_0, black dashed lines) is contoured every 0.5 kg m^{-3}, with selected contours labeled. The freezing line is also shown (pink).

than the inner. The model, in contrast, is convergent—the inner location direction is more southerly than the outer. All modeled velocities are faster than their measured equivalents. The short inner record is least different, with the observations ~15% slower than the model. At the outer location, the long observation record is ~30% slower than the model. The value is similar for the two shorter outer records.

3.2. Transports

The model section across the shelf (Figure 11; location shown in Figure 1) illustrates the shape and the seasonal variability of the EGCC as a surface-intensified jet, similar to the original description by *Bacon et al.* [2002]. Figure 11 shows the means over model years 2000–2007 of winter (DJF) and summer (JJA) temperature, salinity, density (σ_0), the along-stream component of velocity, and sea ice thickness and concentration (fraction). The polar waters exist on the shelf throughout the year, although their low temperatures are modified near surface in summer by seasonal surface warming. This might explain why *Murray et al.* [2010] did not always see the EGCC in satellite sea surface temperature observations. The EGCC currents at the location of the inner mooring are stronger throughout the year than at the outer location, and they are stronger in winter than in summer, in agreement with the measurements (Figure 10). In winter, the EGCC is narrower, faster, and deeper than in summer. Considering the surface and near-surface salinities, the shallowest moored measurements do not capture the shallowest, freshest waters resulting from mid-summer sea ice melt. Nevertheless, the modeled summer (JJA) minimum mean surface salinity of 31.6 agrees with published summer surface salinity measurements [e.g., *Bacon et al.*, 2002; *Sutherland and Pickart*, 2008].

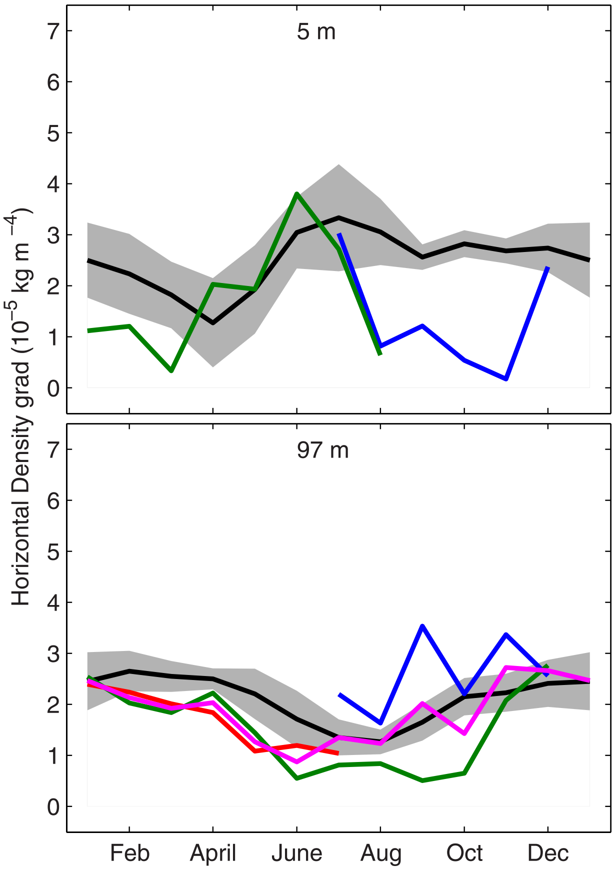

Figure 9. Annual cycle of horizontal density gradients at two depths (labeled). Model mean (thick black) ± 1 SD (gray envelope). Measurements are mean (pink), 2001 (blue), 2002 (green), and 2003 (red).

Measurements from the two moorings are insufficient to calculate EGCC seawater and freshwater transports. However, having established the credibility of the model, we calculate these quantities from the model by integrating eastward along the model section from the coast to 40.5°W, stopping short of the East Greenland Current further offshore (Figures 11e and 11f; at ~60 km). Ocean freshwater transports are calculated with reference to salinities of 35.0 [*Bacon*, 1997] and 34.8 [*Sutherland and Pickart*, 2008]. Results are presented in Figure 12 as a single annual cycle calculated as monthly means ± 1 SD over the chosen model period (2000–2007). Seawater transport is a minimum in August at 1.9 ± 0.3 Sv, similar to the transport measured at this location by *Sutherland and Pickart* [2008] of ~2.2 Sv in August 2004. The modeled winter maximum of 3.8 ± 0.6 Sv occurs in February. The associated seasonal cycle of freshwater transport shows an annual mean, referenced to 35.0 (34.8) of 84 (67) mSv, with summer minimum 59 (47) mSv (August-September mean), and winter maximum 106 (85) mSv (February-March mean). The summer freshwater transport is consistent with the compendium of (summertime) estimates described in *Wilkinson and Bacon* [2005].

The sea ice freshwater flux appears different to the seawater flux (Figure 12). Note that since the model sea ice is ascribed a fixed salinity of 6 in the model, this means that conversion from seawater to freshwater flux is achieved by a fixed multiplying factor $f = (S_{ref}-S)/S_{ref}$, where S_{ref} is the reference salinity, and $S = 6$, so $f = 0.828$ for $S_{ref} = 34.8$ and 0.829 for $S_{ref} = 35.0$; therefore, only one of these (the former) is plotted. Sea ice transports at our study location are near zero in late summer, autumn, and early winter, rising to a maximum in April–May, then declining into summer. This behavior reflects the winter maximum Arctic ice discharge through Fram Strait and the time for its subsequent transit down the east coast of Greenland, consistent with satellite observations of concentration and extent [e.g., *Gloersen et al.*, 1992], and for the same summer period [*Murray et al.*, 2010]. The peak sea ice freshwater flux at the section location is large, at 44 mSv, but it is only substantially present for about half of the year, so its annual mean of 13 mSv is modest. The total annual mean freshwater flux referenced to 35.0 (34.8) is then 97 (80) mSv, to which sea ice contributes 13 (17)%.

A quantitative assessment of the model sea ice freshwater flux is not possible due to the lack of local sea ice thickness measurements. However, using the Hadley Centre Sea Ice and Sea Surface Temperature

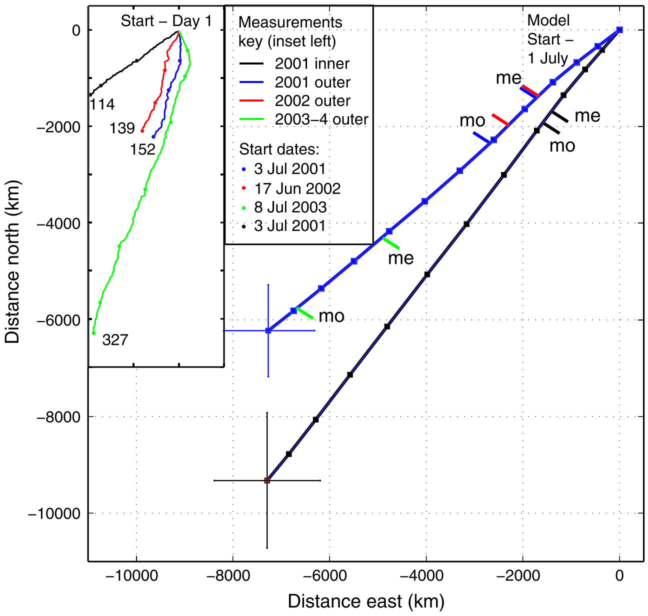

Figure 10. Progressive vector diagrams. (inset) For the four current meter deployments, for each of which, every 50 days are marked, with the final day labeled by elapsed number of days; instruments and start dates are identified in the key. Main plot: for the virtual moorings, inner (black) and outer (blue), for the model mean year starting 1 July; the end of each 30 day model month and ±1 SD in final position are marked. Measured (me) and equivalent modeled (mo) displacements are shown by short projecting bars, colored as in the inset key. Modeled displacements are calculated using the measured durations.

(HadISST) data set [*Rayner et al.*, 2003], we are able to compare modeled sea ice concentration (fraction) with measurements (Figures 11g and 11h). HadISST data are presented on a 1° × 1° geographical grid, so our study area is only represented by one grid point. Nevertheless, seasonal means of modeled and measured sea ice concentration differ by only ~10%. On the one hand, this lends credibility to our modeled representation of sea ice; on the other hand, given that the liquid component of freshwater flux at our study location clearly dominates the solid component, uncertainty in modeled sea ice thickness does not significantly impact our modeled freshwater fluxes.

4. Discussion and Conclusions

The only previous study to examine model representation of the EGCC is by *Treguier et al*. [2005]. They analyzed three GCMs for their performance regarding the EGCC. Two of them had no EGCC at all. The reasons for absence are stated to be (i) incorrect (too shallow) shelf topography and (ii) inadequate vertical resolution that only allowed the mixed layer to exist on the shelf. One model that did support an EGCC had a sensible seawater transport (2.6 Sv at Cape Farewell), but the freshwater transport was much too weak, of order 13 mSv, the stated reason being that shelf salinities were too high. The low freshwater flux may have been due to lack of coupled sea ice models and that the seawater transport was wind forced. The present study shows that our model supports a realistic EGCC, with strengths and weaknesses, so in this section, we will consider (i) aspects of the operation of the model and (ii) whether the model can cast light on the dependence of EGCC strength on forcing.

4.1. Consequences of Uncertainties

We have shown in section 3 that the model generates unidirectional along-shelf flow in the EGCC, a view largely supported by the measured currents, with the exception that offshore (but not reversed) flow is seen to occur in summertime, at least at the outer location. *Mernild et al*. [2006, their Figure 2] show in situ measurements of wind speed and direction from a location close to the mooring sites, spanning the same time period. The clear picture that arises is of largely bimodal directionality: strong north-easterly winds in winter, and lighter winds that are more variable in direction, but mainly south-westerly in summer, with both directions occurring, and at intermediate wind speeds, in spring and autumn. It is now recognized that the presence of Greenland impacts the regional, subsynoptic atmospheric circulation through tip jets and barrier winds [see, e.g., *Renfrew et al*., 2009]. We suggest that aspects of the low model variability result from the relatively coarse spatial scale of the atmospheric forcing, at 1° × 1°, which does not support such features well.

A substantial literature on the physics of buoyant coastal gravity plumes has developed over recent years. The approach can be summarized in three papers (and references therein): *Lentz and Helfrich* [2002], describing the buoyancy-only case; and two papers which analyze the consequences of the inclusion of wind stress—*Lentz* [2004], which treats the case of upwelling-favorable winds and *Moffat and Lentz* [2012],

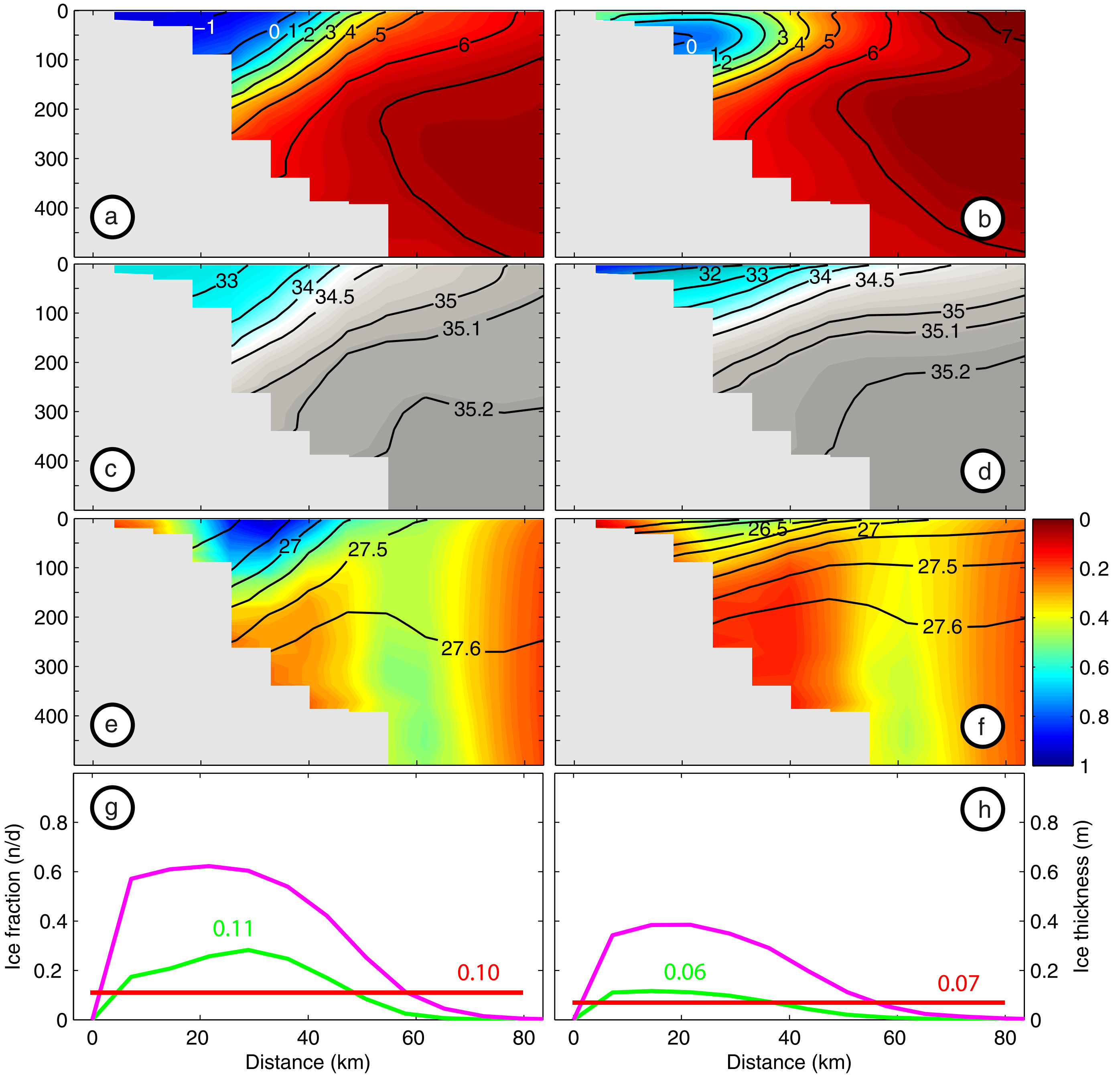

Figure 11. Modeled average sections for 2000–2007, for (left) winter (DJF) and (right) summer (JJA): (a and b) temperature (°C); (c and d) salinity; (e and f) downstream (south-westward, color contours, m s^{-1}) velocities, with density overlay (σ_0, kg m^{-3}); and (g and h) ice fraction (nondimensional; modeled: green; measured: red; numbers show average values) with ice thickness (m, pink).

which treats the downwelling-favorable case. The along-shelf component of the wind stress will set up a secondary, cross-shelf circulation through the action of Ekman transport, leading to upwelling or downwelling near the coast (depending on the wind direction), thereby changing the cross-shelf isopycnal tilt. In spite of the theoretical grounding provided by such analyses, the importance of direct wind forcing on the EGCC is unresolved due to lack of measurements outside summer-autumn, when the EGCC is accessible to research vessels.

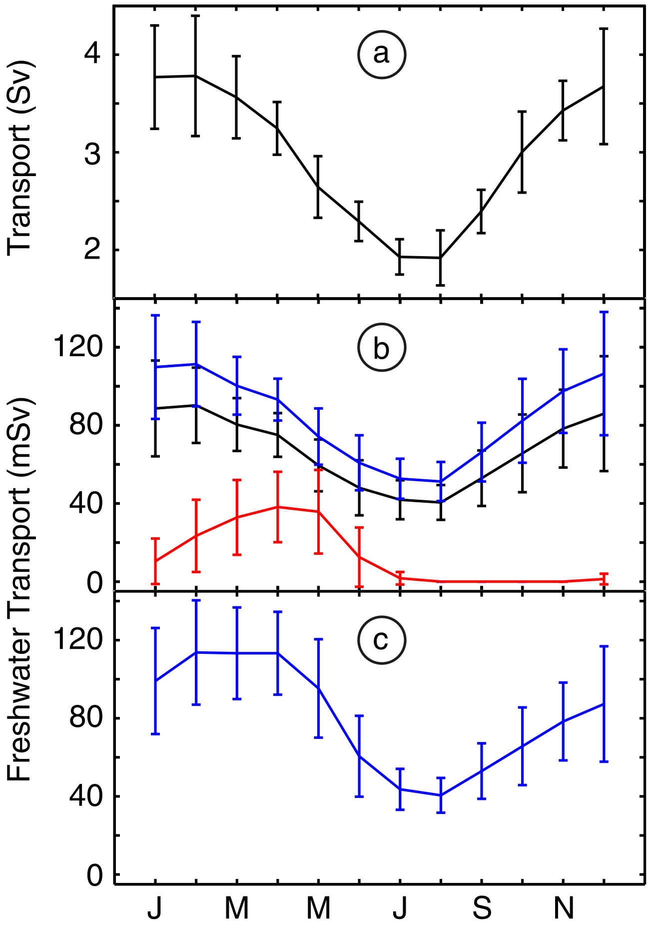

Figure 12. Modeled annual cycles (monthly mean ± 1 SD) of: (a) seawater transport (Sv); (b) transports (mSv) of liquid freshwater referenced to 34.8 (black) and to 35.0 (blue), with sea ice freshwater transport (red); and (c) total freshwater transport (sea ice plus liquid transport referenced to 34.8).

Accordingly, we now examine the modeled cross-shelf circulation. Figure 13 shows summer (JJA) and winter (DJF) vertical velocity across the model section, along with the derived cross-shelf stream function, which shows that the model EGCC is at all times in downwelling-favorable mode, with the winter downwelling strength nearly double that of summer. Modeled cross-shelf velocities (directed shoreward; not shown) are a maximum of 17 (10) cm s^{-1} in winter (summer) and are faster at the location of the outer mooring than the inner. This would lead to the modeled convergent current directions (Figure 10), since downwelling-favorable winds are bound to create a cross-shelf circulation which weakens shoreward at the surface. A reasonable hypothesis for the difference between measured and modeled inner and outer current directions is that topographic steering might be the cause of the measured divergence and that the questionable state of knowledge of the east Greenland shelf bathymetry translates into inaccuracies in details of model bathymetry.

We can pursue the difference between measured and modeled currents (speculatively) one step further. The observed winter (summer) along-shelf currents are ~30 (18) cm s^{-1}. The modeled currents at the outer location are directed ~18° to the right of those from the "straight" part of the long observed record. This is equivalent to a deviation caused by a cross-shelf current component of 10 (6) cm s^{-1}. This implies that the modeled cross-shelf velocities are too fast by (approximately) a factor of 2. We have already noted that the modeled along-shelf velocities are faster than observations by ~50%. Taken together, these points suggest that the transfer of momentum from atmosphere to ocean is too strong. We further suggest that this may (at least in part) be due to the model's representation of air-ice and ice-ocean surface stresses. In section 3 (Figure 9), we noted that while the model's representation of horizontal density gradients at depth was remarkably accurate in comparison with observations, the discrepancy between the two occurred between March and June when the model gradients were higher than measured. This is also when the modeled sea ice concentration was highest (e.g., Figure 12b).

4.2. Buoyancy Versus Wind Forcing

We will next attempt to quantify the relative importance of buoyancy and wind forcing to the EGCC. *Sutherland and Pickart* [2008] used the methods of *Whitney and Garvine* [2005], and we now repeat their analysis for the full EGCC annual cycle in the model. In brief, the wind-forced component of along-shelf velocity (u_w) is characterized by a cross-shelf gradient in sea surface height, and the buoyancy-driven component of along-shelf velocity (u_b) is characterized by a cross-shelf density gradient. Given the spatial configuration of

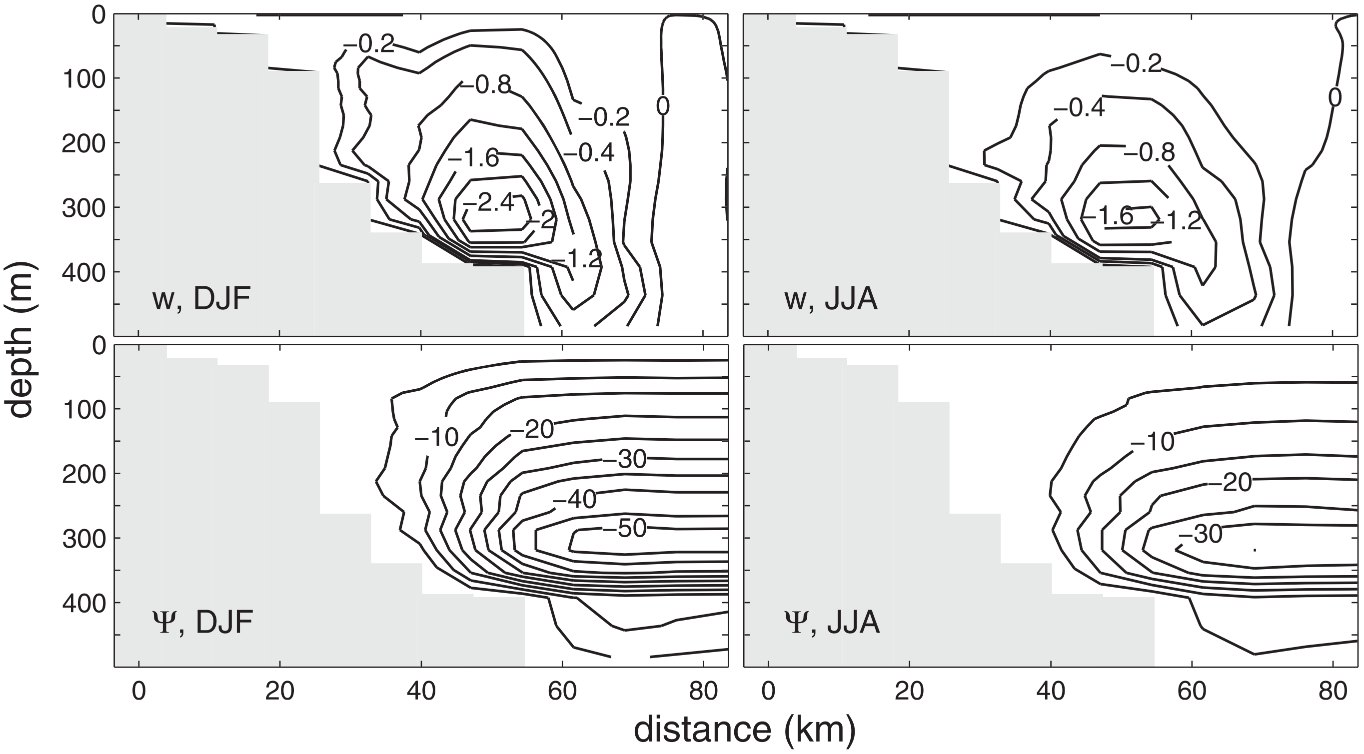

Figure 13. Modeled vertical velocities (w, mm s^{-1}) and cross-shelf stream function (Ψ, m^2 s^{-1}) for winter (DJF) and summer (JJA).

the polar water layer (Figure 11) and for roughly north-easterly winds, both along-shelf velocity components are directed equatorward. The buoyancy-forced velocity component u_b is:

$$u_b = \frac{R_1}{W}\left(2g'Qf\right)^{1/4} \tag{1}$$

where W is the width of the EGCC, R_1 is the first baroclinic Rossby radius, g' is the reduced gravity, Q is the (seawater) volume transport, and $f = 1.3 \times 10^{-4}\ s^{-1}$ is the Coriolis parameter. Parameters are calculated as follows. For each 5 day model output period, the center of the current is located as the current maximum. The width W is estimated as the distance between points either side of the maximum where the current speed falls to 70% of the maximum. This choice was determined by the desire to avoid inclusion of the East Greenland Current (see Figures 11e and 11f). The densities at these two points and at 75 m depth, ρ_1 and ρ_2, are used to estimate $g' = g(\rho_2 - \rho_1)/\rho_1$. The choice of depth (75 m) was determined by the need to select a depth which is representative of the bulk cross-stream density gradient (Figures 11e and 11f) and to avoid the thin near-surface layer, where horizontal (cross stream) density variability is large. The cross-stream density gradient is quite insensitive to choice of depth. EGCC seawater transports Q are calculated between the coast and 40.5°W and from surface to bottom. R_1 is estimated at the location of the current maximum using the WKB approximation [e.g., *Gill*, 1982], whereby $R_1 \approx NH/(f\pi)$, H is the water depth (330 m), and N, the buoyancy frequency, is $N^2 = -(g/\rho)(\partial\rho/\partial z)$; $(\partial\rho/\partial z)$ is approximated as surface-to-bottom density difference divided by H.

The wind-forced velocity component u_w is derived by equating surface (τ_s) and bottom (τ_b) stresses. However, the open-ocean surface stress formulation must be modified to account for (partial) sea ice cover:

$$\tau_s = (1-\phi)\tau_s^o + \phi\tau_s^i \tag{2}$$

where ϕ is the ice cover fraction (cf. Figures 11g and 11h), and τ_s^o and τ_s^i are the atmosphere-ocean and ice-ocean stresses, respectively. In NEMO, the stress formulations are as follows.

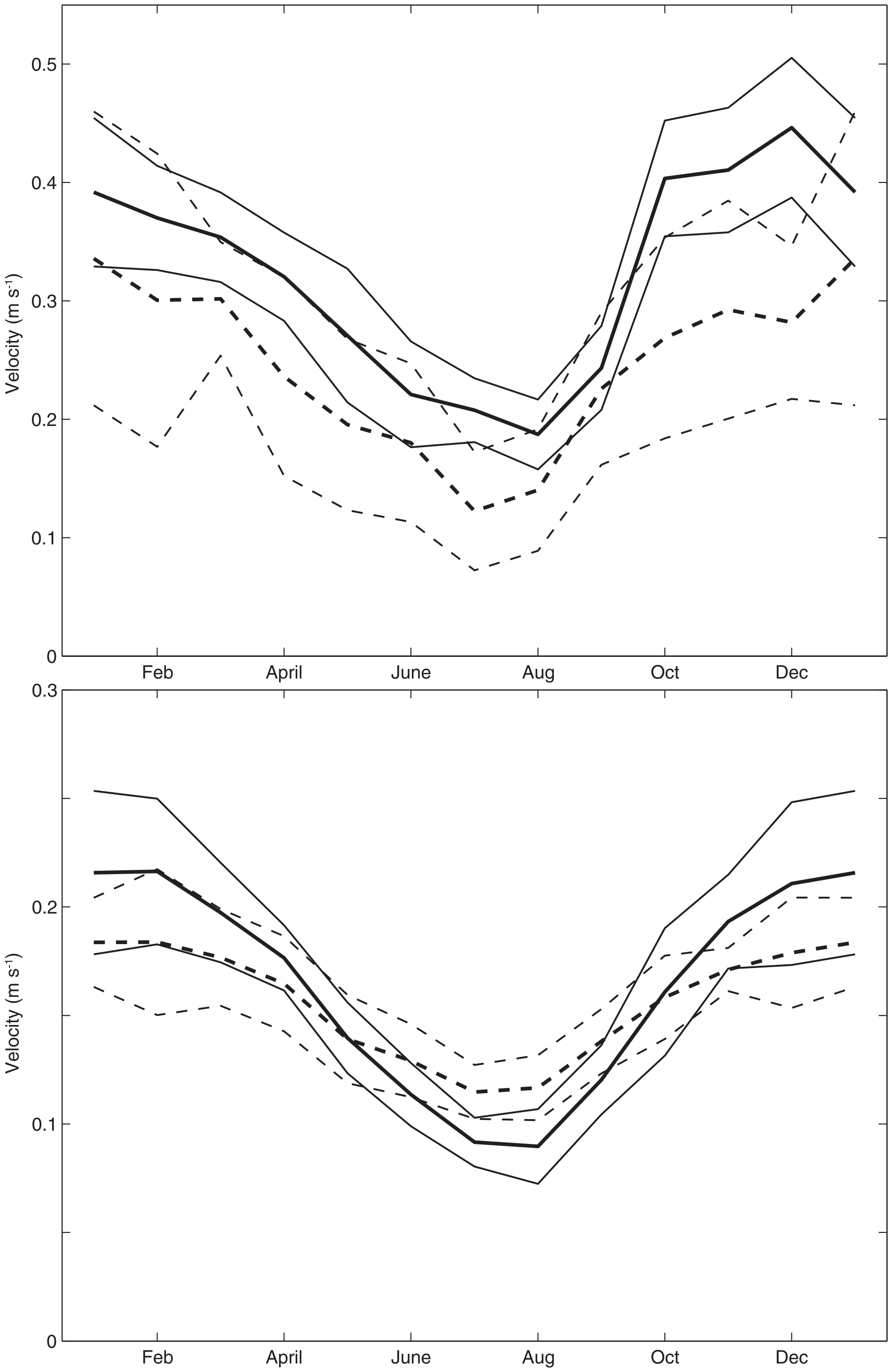

Figure 14. (top) Annual cycle of buoyancy-driven (u_b, solid) and wind-driven (u_w, dashed) parametric velocity components (m s^{-1}), with ±1 SD uncertainty (thin lines); (bottom) area-scaled model transports shown as velocities, for transport due to the bottom current (dashed) and transport referenced to zero at the bottom (solid), with ±1 SD uncertainty (thin lines).

$$\tau_s^o = \rho_{air} C_{10} U^2 \tag{3}$$

where ρ_{air} is air density, C_{10} is the drag coefficient, and U the 10 m neutral wind speed. The drag coefficient is formulated, after *Large and Yeager* [2004], as

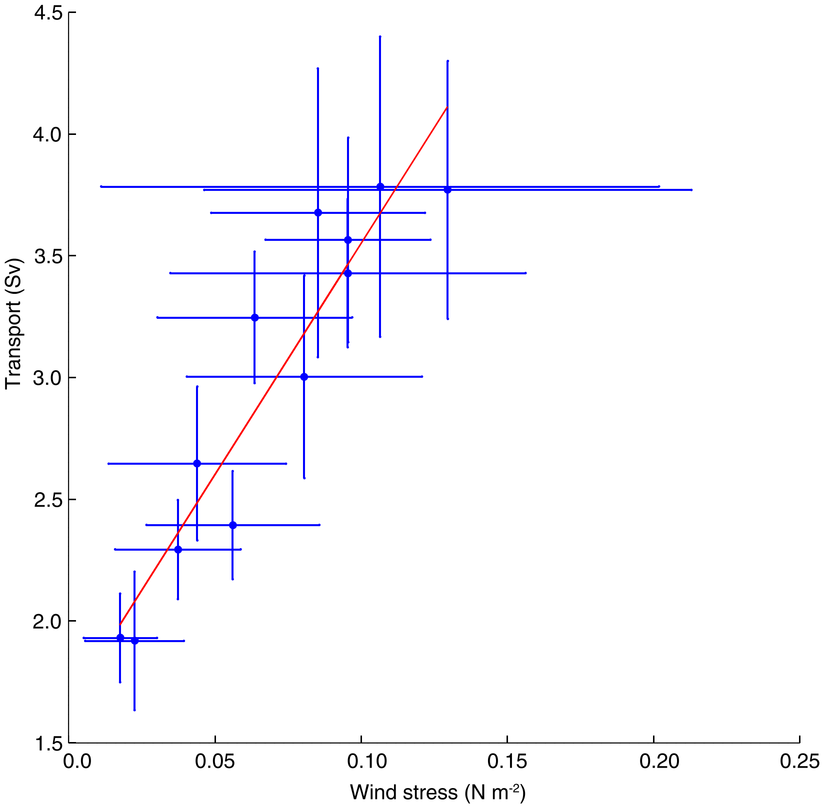

Figure 15. Model mean monthly EGCC seawater transport versus surface wind stress (±1 SD), with linear fit (red).

$$C_{10}=10^{-3}\left(\frac{2.7}{U}+0.142+\frac{U}{13.09}\right) \tag{4}$$

The ice-ocean stress τ_s^i is similarly formulated to equation (3) except that the density is that of ice, the drag coefficient is a constant (5×10^{-3}), and wind speed is replaced by the difference between ice and water speeds. The bottom stress τ_b is

$$\tau_b=\rho C_B\left(u_B^2+e_B^2\right)^{1/2}u_B \tag{5}$$

where ρ is water density, C_B is the bottom drag coefficient, set to a constant (10^{-3}), u_B is the bottom velocity and e_B^2 is the background bottom turbulent kinetic energy, set to a constant (10^{-3} m^2 s^{-2}). We proceed, analogously to *Whitney and Garvine* [2005], by equating (2) and (5), noting that $u_w\equiv u_B$, and neglecting e_B

$$u_w=\left[\frac{1}{\rho C_B}\left\{(1-\phi)\tau_s^o+\phi\tau_s^i\right\}\right]^{1/2} \tag{6}$$

Key inputs to u_w and u_b are as follows. The net surface stress (ice plus ocean) ranges from 0.21 to 0.03 N m^{-2} (January and July, respectively). The Rossby radius R_1 varies from a minimum of 3.4 km (August) to a maximum of 4.5 km (October). It is >4 km October-April and <4 km May-September. The width W is a maximum of 23.6 km (June, August) and a minimum of 14.5 km (December). The ratio R_1/W (the inverse Kelvin number) exerts some control on the magnitude of u_b; the ratio is a maximum in December (0.285) and a minimum in June (0.157), and much of the variability resides in W. Seawater transport Q and reduced-gravity g' are both a maximum in February (3.8 Sv, 0.0079 m s^{-2}) and a minimum in August (1.9 Sv, 0.0056 m s^{-2}). The buoyancy component u_b is relatively insensitive to variations in the quantities in the bracket in equation (1) due to the presence of the 1/4 power, and also the Rossby radius varies little. The most important control on variations in u_b is exerted by the estimate of W.

The results of calculating both u_b and u_w (±1 SD, derived from the eight input years to the monthly mean) from model values are shown in Figure 14. It is seen that both components (wind and buoyancy) are of similar importance. Both have similar seasonal cycles, and the strength of both is roughly doubled in winter compared with summer.

This outcome is interesting but it is also to some extent unsatisfactory. The wind-driven, cross-shelf secondary circulation causes changes in isopycnal tilt. In the present model, we only see the result of downwelling-favorable winds, which therefore modulate greater or lesser *increases* in isopycnal tilt above a "buoyancy-only" baseline, and so cause greater or lesser increases in geostrophic shear. This modulation has been called an "indirect" effect of the wind forcing, but we prefer to call it a *coupled* mode of variability, where the coupling is between buoyancy and wind.

We empirically separate transports into two parts: one due to the bottom current, and one due to the vertical current profile referenced to zero current at the bottom. The former comprises the wind-only part, the latter contains both the buoyancy-only and coupled parts (and any other influences). This calculation is a check on our choices of parameters for the *Whitney and Garvine* [2005] approach. We scale transports into velocities using a nominal cross-sectional area for the shelf waters of 10^7 m^2 (Figure 14). The two different analyses—the parametric approach of *Whitney and Garvine* [2005] and our empirical approach—generate similar outcomes, with similar relative sizes of wind and buoyancy components, and of the annual cycles. Considering the empirical separation (Figure 14), we find winter (summer) total transports of 4.0 (2.1) Sv separate into 2.2 (0.9) Sv due to the buoyancy-plus-coupled part and 1.8 (1.2) Sv due to the wind-only part.

We note that the magnitudes of the currents calculated from the two approaches are different by a factor ~2 (Figure 14), but we have not attempted to "tune" these results, because there is a degree of arbitrariness in both calculations that controls the outcomes. The *Whitney and Garvine* [2005] approach is based on a two-layer system, which we implicitly generalize to the model's quasi-continuous density stratification, so the definition of the current width W contains some flexibility. Also, the scaling of transports into velocities contains some arbitrariness over choice of cross-sectional area A.

If we make the simple assumption that the summer minimum buoyancy-plus-coupled transport of 0.9 Sv does represent the buoyancy-only EGCC, then we can conclude that the difference between winter and summer values ($2.2 - 0.9 = 1.3$ Sv) represents the coupled part due to increased wintertime isopycnal tilt, which implies that the buoyancy-only and coupled parts are of similar magnitudes in winter.

However, these results—from a local study within a GCM—are not unambiguous. We show this by attempting to isolate the buoyancy-only component after the style of *Sutherland and Pickart* [2008]. We plot monthly mean wind stress versus total EGCC transport (Figure 15) and then calculate by linear extrapolation the transport equivalent to zero wind stress. At this value, both wind-only and coupled transports should be zero. This results in what should be a buoyancy-only transport of ~1.6 Sv. However, the model's summertime minimum wind stress is near zero (~0.02 N m^{-2}; Figure 15), and the extrapolation to zero reduces the minimum transport only a little. We note further that the modeled summer cross-shelf transport is still significant (Figure 13), even given low summertime wind stress. The nonzero summertime bottom and cross-shelf currents are probably not due to local wind forcing because they are stronger than the near-zero surface wind stresses would imply.

Furthermore, the wintertime increase in geostrophic shear may result from effects other than the cross-shelf circulation. We know that local near-surface densities increase from summer to winter through local buoyancy loss, and through advection from upstream of denser near-surface waters that have already experienced buoyancy loss. We also know from both model and measurements that the buoyancy loss causes the near-surface horizontal density gradient to decrease from summer to winter (Figure 9), and therefore the near-surface geostrophic shear will decrease, causing in turn a relative reduction in the near-surface contribution to the total transport. Advection of denser near-surface water inshore (and mixing downward) by the cross-shelf circulation will also tend to reduce stratification. The assumption that the wintertime increase in baroclinic transport is solely due to isopycnal tilting results in an underestimate because the surface-forced buoyancy decrease can only reduce the transport.

4.3. Conclusions

We summarize in terms of the aims stated in section 1. First, we have described the data set from the East Greenland shelf. Second, the measurements have shown that our GCM supports a realistic EGCC. Third, we have used the model to calculate EGCC seawater transport, which is a maximum (minimum) in February (August), at 3.8 (1.9) Sv. Freshwater transport, including modeled estimates of sea ice transport and referenced to salinity 35.0, is a maximum (minimum) in February (August) at 106 (59) mSv. Fourth, the model results show that wind and buoyancy forcing are of equal importance to EGCC transport, and an empirical decomposition of the buoyancy-forced transport into a buoyancy-only component and a coupled wind and buoyancy component indicates the two to be of similar magnitude in winter.

The combination of moored measurements with high-resolution model output has established the seasonal evolution of the EGCC at one particular location. The current exists throughout the year and is stronger in winter than in summer. The model winter EGCC freshwater transport is roughly double the summer value, so that the annual mean, ∼80–90 mSv, approaches 50% of the net rate of Arctic freshwater gain [*Tsubouchi et al*., 2012], underlining the climatic importance of the EGCC and the need for further understanding. In future work, we will investigate the factors controlling the EGCC's sources, variability, and downstream continuity.

Acknowledgments
The authors wish to thank the anonymous reviewers for their helpful comments and their patience. The University of Hamburg and CEFAS carried out the mooring deployment and recoveries, with thanks to ships crew, chief scientists (Jürgen Holfort, John Mortensen, and Detlef Quadfasel), and mooring technicians (Ulrich Drübbisch, Andreas Welsch, John Read, and Neil Needham), supported by the EU fifth Framework Program Arctic-Subarctic Ocean Fluxes project, the EU sixth Framework Program DAMOCLES project, WHOI-OCCI, and the UK Department for Environment, Food and Rural Affairs (DEFRA) projects, SD0440 and ACME-ME5102. Our thanks also go to Andrew Coward and Beverly de Cuevas for extracting and compiling the NEMO output. This study was funded by the UK Natural Environment Research Council and is a contribution to the Arctic Research Programme TEA-COSI project. We acknowledge the use of the UK National High-Performance Computing resource.

References

Bacon, S. (1997), Circulation and fluxes in the North Atlantic between Greenland and Ireland, *J. Phys. Oceanogr.*, *27*, 1420–1435.

Bacon, S., G. Reverdin, I. Rigor, and H. Snaith (2002), A freshwater jet on the east Greenland shelf, *J. Geophys. Res.*, *107*(C7), 3068, doi:10.1029/2001JC000935.

Bacon, S., P. Myers, B. Rudels, and D. Sutherland (2008), Accessing the inaccessible: Buoyancy driven coastal currents on the shelves of Greenland and eastern Canada, in *Arctic–Subarctic Ocean Fluxes: Defining the Role of the Northern Seas in Climate*, edited by R. R. Dickson, J. Meincke, and P. Rhines, chap. 28, pp. 701–720, Springer, Berlin.

Barnier, B., et al. (2006), Impact of partial steps and momentum advection schemes in a global ocean circulation model at eddy permitting resolution, *Ocean Dyn.*, *56*, 543–567.

Brodeau, L., B. Barnier, A.-M. Treguier, T. Penduff, and S. Gulev (2010), An ERA40-based atmospheric forcing for global ocean circulation models, *Ocean Modell.*, *31*(3–4), 88–104.

Cox, K., J. Stanford, A. McVicar, E. Rohling, K. Heywood, S. Bacon, M. Bolshaw, P. Dodd, S. de la Rosa, and D. Wilkinson (2010), Interannual variability of Arctic sea ice export into the East Greenland Current, *J. Geophys. Res.*, *115*, C12063, doi:10.1029/2010JC006227.

Daniault, N., H. Mercier, and P. Lherminier (2011), The 1992–2009 transport variability of the East Greenland-Irminger Current at 60°N, *Geophys. Res. Lett.*, *38*, L07601, doi:10.1029/2011GL046863.

Dickson, R., B. Rudels, S. Dye, M. Karcher, J. Meincke, and I. Yashayaev (2007), Current estimates of freshwater flux through Arctic and subarctic seas, *Prog. Oceanogr.*, *73*, 210–230.

Dietrich, G. (1969), Atlas of the hydrography of the northern North Atlantic Ocean, 140 pp., Int. Counc. for the Explor. of the Seas, Charlottenlund Slot, Denmark.

Fichefet, T., and M. M. Maqueda (1997), Sensitivity of a global sea ice model to the treatment of ice thermodynamics and dynamics, *J. Geophys. Res.*, *102*, 12,609–12,646.

Gill, A. E. (1982), *Atmosphere-Ocean Dynamics*, Academic Press, London.

Gloersen, P., W. J. Campbell, D. J. Cavalieri, J. C. Comiso, C. L. Parkinson, and H. J. Zwally (1992), Arctic and Antarctic sea ice, 1978–1987: satellite passive-microwave observations and analysis, NASA SP-511, NASA, Washington D. C.

Holfort, J., and J. Meincke (2005), Time series of freshwater transport on the East Greenland shelf at 74°N, *Meteorol. Z.*, *14*, 703–710.

Holfort, J., E. Hansen, S. Østerhus, S. Dye, S. Jonsson, J. Meincke, J. Mortensen, and M. Meredith (2008), Freshwater fluxes east of Greenland, in *Arctic–Subarctic Ocean Fluxes: Defining the Role of the Northern Seas in Climate*, edited by R. R. Dickson, J. Meincke, and P. Rhines, chap. 11, pp. 263–287, Springer, Berlin.

Holliday, N. P., A. Meyer, S. Bacon, S. G. Alderson, and B. de Cuevas (2007), Retroflection of part of the east Greenland current at Cape Farewell, *Geophys. Res. Lett.*, *34*, L07609, doi:10.1029/2006GL029085.

Jakobsson, M., R. Macnab, L. Mayer, R. Anderson, M. Edwards, J. Hatzky, H. W. Schenke, and P. Johnson (2008), An improved bathymetric portrayal of the Arctic Ocean: Implications for ocean modeling and geological, geophysical and oceanographic analyses, *Geophys. Res. Lett.*, *35*, L07602, doi:10.1029/2008GL033520.

Koenigk, T., U. Mikolajewicz, H. Haak, and J. Jungclaus (2007), Arctic freshwater export in the 20th and 21st centuries, *J. Geophys. Res.*, *112*, G04S41, doi:10.1029/2006JG000274.

Large, W. G., and S. G. Yeager (2004), Diurnal to decadal global forcing for ocean and sea-ice models: The data sets and flux climatologies, *Tech. Note NCAR/TN-460+STR*, Natl. Cent. for Atmos. Res., Boulder, Colo.

Lentz, S. (2004), The response of buoyant coastal plumes to upwelling-favorable winds, *J. Phys. Oceanogr.*, *34*, 2458–2469.

Lentz, S., and K. R. Helfrich (2002), Buoyant gravity current along a sloping bottom in a rotating fluid, *J. Fluid Mech.*, *464*, 251–278.

Levier, B., A.-M. Treguier, G. Madec, and V. Garnier (2007), Free surface and variable volume in the NEMO code, *MERSEA IP Rep. WP09-CNRS-STR-03-1A*, 47 pp., IFREMER, Brest, France.

Levitus, S., T. Boyer, M. Conkright, T. O' Brien, J. Antonov, C. Stephens, L. Stathoplos, D. Johnson, and R. Gelfeld (1998a), *NOAA Atlas NESDIS 18, World Ocean Database 1998, Introduction*, vol. 1, U.S. Gov. Print. Off., Washington, D. C.

Levitus, S., T. Boyer, M. Conkright, D. Johnson, T. O' Brien, J. Antonov, C. Stephens, and R. Gelfeld (1998b), *NOAA Atlas NESDIS 19, World Ocean Database 1998*, *Temporal Distribution of Mechanical Bathythermograph Profiles*, vol. 2, U.S. Gov. Print. Off., Washington, D. C.

Madec, G., and NEMO Team (2011), *NEMO Ocean Engine, Version 3.3, Note du Pole de Modelisation*, Inst. Pierre-Simon Laplace, Paris.

Manabe, S., and R. Stouffer (1995), Simulation of abrupt climate change induced by freshwater input to the North Atlantic Ocean, *Nature*, *378*, 165–167.

Mernild, S. H., G. E. Liston, B. Hasholt, and N. T. Knudsen (2006), Snow distribution and melt modeling for Mittivakkat Glacier, Ammassalik Island, Southeast Greenland, *J. Hydrometeorol.*, *7*, 808–824.

Moffat, C., and S. Lentz (2012), On the response of a buoyant plume to downwelling-favorable wind stress, *42*, 1083–1098, doi:10.1175/JPO-D-11-015.1.

Murray, T., et al. (2010), Ocean regulation hypothesis for glacier dynamics in southeast Greenland and implications for ice sheet mass changes, *J. Geophys. Res.*, *115*, F03026, doi:10.1029/2009JF001522.

Pickart, R., D. Torres, and P. Fratantoni (2005), The East Greenland Spill Jet, *J. Phys. Oceanogr.*, *35*, 1037–1053.

Rayner, N. A., D. E. Parker, E. B. Horton, C. K. Folland, L. V. Alexander, D. P. Rowell, E. C. Kent, and A. Kaplan (2003), Global analyses of sea surface temperature, sea ice, and night marine air temperature since the late nineteenth century, *J. Geophys. Res.*, *108*(D14), 4407, doi:10.1029/2002JD002670.

Renfrew, I. A., G. N. Petersen, D. A. J. Sproson, G. W. K. Moore, H. Adiwidjaja, S. Zhang, and R. North (2009), A comparison of aircraft-based surface-layer observations over Denmark Strait and the Irminger Sea with meteorological analyses and QuikSCAT winds, *Q. J. R. Meteorol. Soc.*, *135*, 2046–2066, doi:10.1002/qj.444.

Rudels, B., E. Fahrbach, J. Meincke, G. Budeus, and P. Eriksson (2002), The East Greenland Current and its contribution to the Denmark Strait Overflow, *ICES J. Mar. Sci.*, *59*, 1133–1154, doi:10.1006/jmsc.2002.1284.

Shepherd, A., et al. (2012), A reconciled estimate of ice-sheet mass balance, *Science*, *338*, 1183–1189, doi:10.1126/science.1228102.

Smith, W., and D. Sandwell (1997), Global sea floor topography from satellite altimetry and ship depth soundings, *Science*, *277*, 1956–1962.

Steele, M., R. Morley, and W. Ermold (2001), PHC: A global ocean hydrography with a high-quality Arctic Ocean, *J. Clim.*, *14*, 2079–2087.

Straneo, F., G. S. Hamilton, D. A. Sutherland, L. A. Stearns, F. Davidson, M. O. Hammill, G. B. Stenson, and A. Rosing-Asvid (2010), Rapid circulation of warm subtropical waters in a major glacial fjord in East Greenland, *Nat. Geosci.*, *3*, 182–186, doi:10.1038/NGEO764.

Sutherland, D., and R. Pickart (2008), The East Greenland Coastal Current: Structure, variability and forcing, *Prog. Oceanogr.*, *78*, 58–77.

Sutherland, D., R. Pickart, E. P. Jones, K. Azetsu-Scott, A. J. Eert, and J. Olafsson (2009), Freshwater composition of the waters off southeast Greenland and their link to the Arctic Ocean, *J. Geophys. Res.*, *114*, C05020, doi:10.1029/2008JC004808.

Sutherland, D. A., F. Straneo, G. B. Stenson, F. J. M. Davidson, M. O. Hammill, and A. Rosing-Asvid (2013), Atlantic water variability on the SE Greenland continental shelf and its relationship to SST and bathymetry, *J. Geophys. Res.*, *118*, 1–9, doi:10.1029/2012JC008354.

Treguier, A.-M., S. Theetten, E. Chassignet, T. Penduff, R. Smith, L. Talley, J. Beismann, and C. Bonin (2005), The North Atlantic Subpolar Gyre in four high-resolution models, *J. Phys. Oceanogr.*, *35*, 757–774.

Tsubouchi, T., S. Bacon, A. C. Naveira Garabato, Y. Askenov, S. Laxon, E. Fahrbach, A. Beszczynska-Möller, E. Hansen, C. Lee, and R. Ingvaldsen (2012), The Arctic Ocean in summer: A quasi-synoptic inverse estimate of boundary fluxes and water mass transformation, *J. Geophys. Res.*, *117*, C01024, doi:10.1029/2011JC007174.

Våge, K., R. S. Pickart, M. A. Spall, G. W. K. Moore, H. Valdimarsson, D. J. Torres, S. Y. Erofeeva, and J. E. Ø. Nilsen (2013), Revised circulation scheme north of Denmark Strait, *Deep Sea Res., Part I*, *79*, 20–39, doi:10.1016/j.dsr.2013.05.007.

Van den Broeke, M., J. Bamber, J. Ettema, E. Rignot, E. Schrama, W. J. van de Berg, E. van Meijgaard, I. Velicogna, and B. Wouters (2009), Partitioning recent Greenland mass loss, *Science*, *326*, 984–986, doi:10.1126/science.1178176.

Velicogna, I. (2009), Increasing rates of ice mass loss from the Greenland and Antarctic ice sheets revealed by GRACE, *Geophys. Res. Lett.*, *36*, L19503, doi:10.1029/2009GL040222.

Whitney, M., and R. Garvine (2005), Wind influence on a coastal buoyant outflow, *J. Geophys. Res.*, *110*, C03014, doi:10.1029/2003JC002261.

Wilkinson, D., and S. Bacon (2005), The spatial and temporal variability of the East Greenland Coastal Current from historic data, *Geophys. Res. Lett.*, *32*, L24618, doi:10.1029/2005GL024232.